
 Received: 22 August 2017, Accepted: 12 December 2017

Edited by: R. Dickman

Reviewed by: A. Peters, Dept. Chemical Engineering, Louisiana Tech Univ., Ruston, USA.

Licence: Creative Commons Attribution 4.0

 DOI: <http://dx.doi.org/10.4279/PIP.100001>



ISSN 1852-4249

Pattern formation mechanisms in sphere-forming diblock copolymer thin films

 Leopoldo R. Gómez,¹ Nicolás A. García,¹ Richard A. Register,² Daniel A. Vega^{1*}

The order–disorder transition of a sphere-forming block copolymer thin film was numerically studied through a Cahn–Hilliard model. Simulations show that the fundamental mechanisms of pattern formation are spinodal decomposition and nucleation and growth. The range of validity of each relaxation process is controlled by the spinodal and order–disorder temperatures. The initial stages of spinodal decomposition are well approximated by a linear analysis of the evolution equation of the system. In the metastable region, the critical size for nucleation diverges upon approaching the order–disorder transition, and reduces to the size of a single domain as the spinodal is approached. Grain boundaries and topological defects inhibit the formation of superheated phases above the order–disorder temperature. The numerical results are in good qualitative agreement with experimental data on sphere-forming diblock copolymer thin films.

I. Introduction

Many practical applications of polymers and other soft matter involve the self-assembly of the system into complex multidomain morphologies [1]. The final properties and applications of such materials depend on the ability to control the morphology by adjusting molecular features and macroscopic variables. For example, by appropriate control over their molecular architecture, block copolymers can be designed as rigid and transparent thermoplastics, or as soft and flexible elastomers, depending on the features of their building blocks [1].

The most important features of the block copolymer phase behavior are already captured by the simplest A–B diblock architecture [1, 2]. Here, the unfavorable interactions between blocks, and the constraints imposed

by the connectivity between their constituents, results in a nanophase separation leading to the formation of periodic morphologies. For example, depending on molecular size, temperature, and relative volume fraction of the two blocks, diblock copolymer melts can develop body-centered-cubic (BCC) arrays of spheres, hexagonal patterns of cylinders, gyroids, or lamellar structures. For these systems, the periodicity of the self-assembled pattern is mainly controlled by the average molecular weight, and typically is in the range of 10–100 nm. Also, since the magnitude of the interblock repulsive interaction generally diminishes with temperature, an order–disorder transition can be induced thermally at the order–disorder transition temperature T_{ODT} [1, 2].

During recent decades, the properties of self-assembling copolymers have received great attention because of their potential use in nanotechnology [3–10]. Applications of block copolymer systems include, among others, templates for nanoporous materials, solar cells, and photonic crystals. Perhaps the most pressing application for understanding pattern formation in two-dimensional thin film systems is block copolymer lithography [6–9]. This process uses self-assembled patterns, such as single layers of cylinders or spheres in

*E-mail: dvega@uns.edu.ar

¹ Instituto de Física del Sur (IFISUR), Consejo Nacional de Investigaciones Científicas y Técnicas (CONICET), Universidad Nacional del Sur, 8000 Bahía Blanca, Argentina.

² Department of Chemical and Biological Engineering, Princeton University, Princeton, New Jersey, 08544, USA.

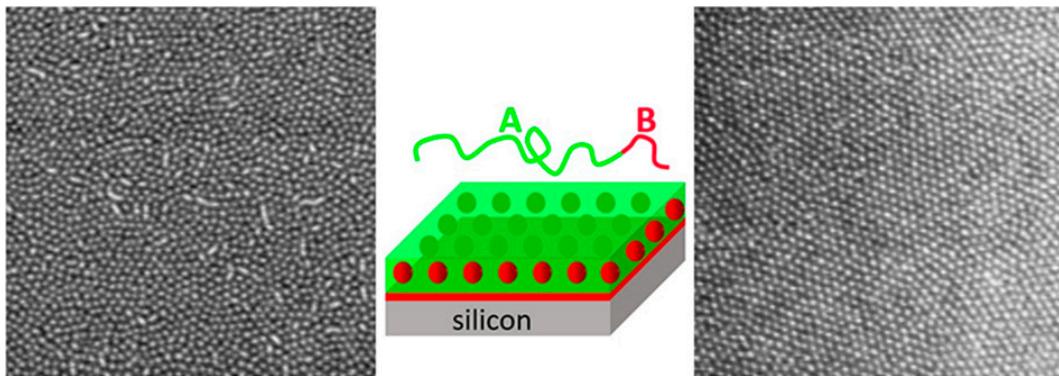


Figure 1: AFM phase images of the PS-PEP block copolymer thin film supported on a silicon substrate after annealing at $T = 333$ K. Left and right panels show the pattern configuration after 5 minutes and 255 minutes of thermal annealing, respectively. Image size: $1.0 \mu\text{m} \times 1.0 \mu\text{m}$. The schematic in the central panel shows the block copolymer configuration in the thin film. Here, the minority phase (polystyrene) forms hexagonally-packed arrays of nearly spherical domains (red domains in the scheme). Note the presence of a wetting layer of PS blocks on the silicon substrate.

copolymer thin films, as templates to fabricate devices at the nanometer length scale. However, the use of these materials to obtain lithographic masks requires the production of structures with long-range order. Since the degree of ordering is controlled mainly by the density of topological defects, it is important to determine the physical mechanisms involved in the nanophase separation process and the effects of the thermal history on the pattern morphology.

Experimentally, the time evolution of the density of topological defects and correlation lengths at $T < T_{\text{ODT}}$ has been studied through atomic force microscopy (AFM) in block copolymer thin films with different morphologies [11–16]. On the one hand, by comparing the density of disclinations (orientational defects) and the correlation length, it was shown that in cylinders (smectic phase) the dominant mechanism of coarsening involves mostly the annihilation of complex arrays of disclinations [11]. On the other hand, in monolayers of sphere-forming thin films with hexagonal order it was found that the majority of the defects are condensed in grain boundaries [16]. The orientational correlation length was found to grow following a power law, but with a higher exponent than the translational correlation length [16, 17]. However, as the typical exponents observed in the scaling laws of these experimental systems are relatively small ($\sim \frac{1}{5}$ for the translational correlation length and $\frac{1}{4}$ for the orientational correlation length), they are hard to distinguish from logarithmic, glass-like, dynamics [18].

The process of phase separation and the kinetics of ordering in different two-dimensional systems have been studied through different phase field models [17–20]. In particular, simulations of hexagonal systems with a Cahn–Hilliard model were found to be in good agreement with experimental data for block copolymer thin films. Through simulations, it was also shown that the orientational correlation length grows via annihilation of dislocations [17]. In addition, simulations have also shown that triple points, regions where three grains meet, control the dynamics of defect annihilation and can lead to the formation of metastable configurations of domains that slow down the dynamics, with correlation lengths growing logarithmically in time [18].

In block copolymer systems, the degree of order and content of defects depend not only on T_{ODT} , but also on thermal history, depth of quench, and other characteristic temperatures, like the glass transition temperature for each block, the spinodal temperature, and the temperature of crystallization (if any) [1, 2].

In general, in first-order phase transitions, the depth of quench determines whether the system relaxes to equilibrium by means of spinodal decomposition or nucleation and growth [21, 22]. Spinodal decomposition is the relaxation process of a system quenched into an unstable state. In this case the phase transition is a spontaneous process, beginning with the amplification of fluctuations which are small in amplitude but large in extent. Nucleation and growth is the physical mechanism of relaxation emerging when the system is quenched

into a metastable state. This is an activated process, and a free energy barrier must be overcome in order to relax to the stable phase. In polymeric systems both mechanisms can be inhibited due to crystallization or vitrification of any of the copolymer blocks [1].

In this paper, we study the disorder–order transition and the ordering kinetics in sphere-forming block copolymer thin films as a function of the depth of quench. The dynamics are studied through a Cahn–Hilliard equation and compared with experiments on diblock copolymer thin films. We have organized the paper as follows: Section II presents the experimental system. In section III we present the equations of evolution of the order parameter for diblock copolymer systems and the classical linear instability analysis of the Cahn–Hilliard equation. Section III.i describes the numerical scheme employed to solve the model equations. Results and concluding remarks are presented in sections IV and V, respectively.

II. Experimental System

The sphere-forming diblock copolymer used in this work consists of a chain of polystyrene (PS, 3300 g/mol) covalently bonded to a chain of poly(ethylene-alt-propylene) (PEP, 23100 g/mol). The copolymer was synthesized through sequential living anionic polymerization of styrene and isoprene followed by selective saturation of the isoprene block [23]. Because the two polymer species are immiscible, the minority polystyrene forms spherical microdomains within the majority poly(ethylene-alt-propylene). The bulk morphology of the PS-PEP diblock copolymer consists of arrays of spherical domains of PS packed with a BCC order, with $T_{\text{ODT}} = 394 \pm 2$ K, according to small-angle X-ray scattering experiments. The glass transition temperature for the PS block was estimated to be $T_{\text{g}}^{\text{PS}} \sim 320$ K while the glass transition temperature of the PEP block is well below room temperature [24].

The block copolymer was deposited (film thickness ca. 30 nm) on silicon substrates via spin coating from a disordered state in toluene, a good solvent for both blocks, to produce a quasi-two-dimensional periodic hexagonal lattice of polystyrene spheres within a matrix of poly(ethylene-alt-propylene). The film thickness was measured using ellipsometry (Gaertner Scientific LS116S300, $\lambda = 632.8$ nm). Order was induced through vacuum annealing above the glass transition temperature of both blocks and below the T_{ODT} of the

block copolymer. In this system, the PEP block wets the air interface, while PS wets the silicon oxide substrate [25, 26], i.e., there is an asymmetric wetting condition (see schematic in Fig. 1).

Samples were imaged with a Veeco Dimension 3000 AFM in tapping mode, using phase contrast imaging. The contrast is provided by the difference in elastic modulus between the hard polystyrene spheres and the softer poly(ethylene-alt-propylene) blocks. The repeat spacing for the block copolymer is 25 nm (as measured on thin films by AFM). The spring constant of the tip (uncoated Si) was ~ 40 N/m and its resonant frequency 300 kHz.

During spin coating, most of the toluene evaporates rapidly (within a few seconds), so the block copolymer thin film suffers a relatively quick quench well below the glass transition temperature of the PS domains, inhibiting the relaxation of the early nanophase separated structure towards equilibrium. The deep and quick quench below the spinodal and order–disorder temperatures forms a nanodomain structure that contains a high density of defects. Figure 1 shows tapping-mode AFM phase images of the PS-PEP system at a very early stage of annealing. Note in this figure the large content of defects and that the spherical domains are not well defined. On the other hand, after ~ 4 hours of annealing above the glass transition temperature of the PS block, the pattern shows a higher degree of order and a well-defined structure of spherical domains. In order to better quantify the degree of order in this system, here we calculate the orientational order parameter ξ_6 . Using standard image tools to identify the position of the individual spheres and applying a Delaunay triangulation [13, 16] it is possible to determine the inter-sphere bond orientation $\theta(r)$, with regard to a reference axis. Then, we can evaluate the local orientational order parameter at a position \mathbf{r} : $\Phi(\mathbf{r}) = \exp[6i(\theta(\mathbf{r}_1) - \theta(\mathbf{r}_2))]$, where $\mathbf{r} = \mathbf{r}_1 - \mathbf{r}_2$ [17, 18]. The azimuthally-averaged correlation function $g_6(r) = \langle \Phi(\mathbf{r}) \rangle$ was then calculated and the correlation length ξ_6 was measured by fitting $g_6(r)$ with an exponential $\exp(-r/\xi_6)$. Figure 2 shows the azimuthally-averaged correlation function $g_6(r)$ for the two pattern configurations shown in Fig. 1. During annealing, the correlation length of the film increases from $\lesssim 10$ nm to 80 nm upon increasing the annealing time from 5 to 255 minutes.

III. Model

The phase transition and the dynamics of nanophase separation for a diblock copolymer can be described through the Cahn–Hilliard model [1]. A convenient order parameter for the diblock copolymer can be defined in terms of the local volume fractions for each block as $\psi = \phi_A - \phi_B - (1 - 2f)$. Here ϕ_A and ϕ_B are the local densities for the *A* and *B* blocks, respectively, and f is the volume fraction of one block in the copolymer. The dynamics can be described by the following time-dependent equation for a conserved order parameter [27]

$$\frac{\partial \psi}{\partial t} = M \nabla^2 \frac{\delta F\{\psi\}}{\delta \psi}. \quad (1)$$

In this equation, M is a phenomenological mobility coefficient, and $F\{\psi\}$ is the free energy functional. In this model, all the dynamics are rescaled by the mobility coefficient M , which fixes the characteristic timescale of the diffusive phenomena that drive the dynamics towards equilibrium. In block copolymer systems, the diffusion process depends on several parameters, including the monomeric friction coefficients of the individual blocks, molecular weight distribution, composition, symmetry of the mesophase structure, and degree of segregation between blocks [28]. In addition, the diffusion also depends on the molecular architecture

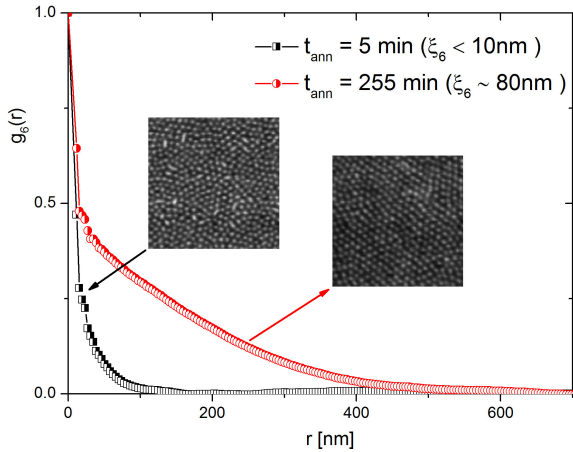


Figure 2: Orientational correlation function $g_6(r)$ for the two patterns shown in Fig. 1. As annealing time increases, there is an increasing order in the system, as shown by the slower decay in $g_6(r)$ with r and the increase in the correlation length ξ_6 .

and degree of entanglement, that dictate whether the relaxation occurs by a Rouse, reptation, or arm retraction mechanism [28–30]. Thus, a detailed description of the dynamics involves an enormous complexity and consequently, at present, there is no phase field model equation like Eq. (1) able to capture all of the controlling parameters. However, as the experiments here are conducted at temperatures well above the glass transition temperatures of both blocks, we found that a constant mobility provides a good approximation to the dynamic response.

In the mean field approximation, the free energy functional for a diblock copolymer can be decomposed into a sum of short-range and long-range terms [31, 32]

$$F\{\psi\} = F_S\{\psi\} + F_L\{\psi\}. \quad (2)$$

The short-range contribution F_S has the form of a Landau free energy and can be expressed as

$$F_S\{\psi\} = \int d\mathbf{r} \{W(\psi) + \frac{1}{2} D (\nabla\psi)^2\}, \quad (3)$$

where $W(\psi)$ represents the mixing free energy of the homogeneous blend of disconnected *A* and *B* homopolymers, the term containing the gradient represents the free energy penalty generated by the spatial variations of ψ (interfacial energy), and D is a parameter related to the Kuhn segment length a_0 and the number fraction of *A* monomers per chain f as: $D = \frac{b^2}{48f(1-f)}$ [33].

The free energy $W(\psi)$ has the form of a non-symmetrical double well

$$W(\psi) = -\frac{1}{2} [\tau - a(1-2f)^2] \psi^2 + \frac{v}{3} \psi^3 + \frac{u}{4} \psi^4. \quad (4)$$

Here, the parameter τ is related to temperature by means of the Flory-Huggins parameter χ through [34, 35]

$$\tau = 8f(1-f)\rho_0\chi - \frac{2s(f)}{f(1-f)N}, \quad (5)$$

where ρ_0 is the monomer density, $N = N_A + N_B$ is the total number of monomers in the diblock copolymer chain, $s(f)$ is a constant of order one [31], $v = \nu(1-2f)$ and $b = \frac{9}{[2Na_0(1-f)]^2}$. Here, a , ν , and u are phenomenological constants derived by Leibler using the random phase approximation [31, 33].

The Flory-Huggins interaction parameter χ measures the incompatibility between the two monomer units and depends on the absolute temperature T as $\chi =$

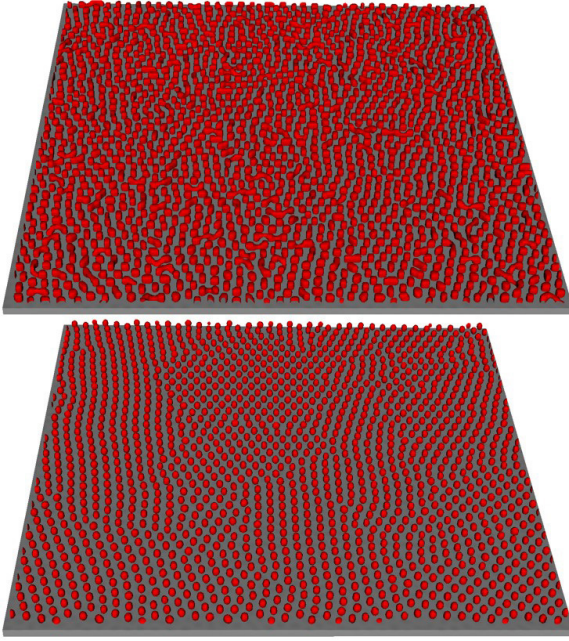


Figure 3: Phase separation process after 4.5×10^4 time steps for a sphere-forming diblock copolymer monolayer quenched within the spinodal region. Top and bottom panels correspond to $\tau_r = \tau/\tau_s - 1 = 0.34$ and $\tau_r = 0.025$, respectively. In order to describe the structure of domains developed by the minority phase, here we employ a contour plot at a fixed value of the order parameter ($\psi = -0.22$).

$A + B/T$, where A and B are phenomenological constants [1]. Thus, note that here τ increases as temperature decreases.

The term $F_L\{\psi\}$, representing the long-range contribution that accounts for the connectivity between blocks, can be expressed as [32]

$$F_L\{\psi\} = \frac{b}{2} \int d\mathbf{r}_1 \int d\mathbf{r}_2 G(\mathbf{r}_1 - \mathbf{r}_2) \psi(\mathbf{r}_1) \psi(\mathbf{r}_2), \quad (6)$$

where G is the solution of $\nabla^2 G(\mathbf{r}) = -\delta(\mathbf{r})$.

Then, using Eqs. (2)–(6), Eq. (1) takes the form

$$\frac{1}{M} \frac{\partial \psi}{\partial t} = \nabla^2 (\tilde{f}(\psi) - D \nabla^2 \psi) - b\psi, \quad (7)$$

where $\tilde{f}(\psi)$ is given by

$$\tilde{f}(\psi) = -[\tau - a(1 - 2f)^2] \psi + v\psi^2 + u\psi^3. \quad (8)$$

Equation (7) is actually a coarse-grained phase field model. In recent years, such models have been used to study a variety of systems under different conditions, including shear and other external fields, curvature and patterned substrates, and pattern formation in 3D [20, 33, 36–40]. In this work, the free energy parameters were selected to capture the desired symmetry and segregation strength of the block copolymer hexagonal phase [20, 34, 35]. More details about the equilibrium phase diagram and the different spinodals can be found elsewhere [34, 35, 41–44].

i. Numerical methods

In this work, Eq. (7) was numerically solved under confinement between impenetrable walls that represent the interfaces with the air and the silicon wafer. To describe the confinement interactions we consider an external field that couples with the two components of the block copolymer system (see details in Ref. [45]). The film thickness was fixed at the monolayer value. We employed periodic boundary conditions along the (x, y) -axis. The evolution equation, Eq. (7), was solved through the cell dynamics method, which has been extensively used in non-equilibrium studies of this kind of system [35]. One of the main advantages of this model is that it is efficient over the time scales involved in the dynamics of defect annihilation, and is thus appropriate to describe the dynamics of coarsening (see Ref. [46] for an extensive and detailed analysis of the cell dynamics method and a comparison with the Cahn–Hilliard–Cook model). Another remarkable advantage of this model is its matricial nature (continuum discretization), which allows the implementation of a transparent parallelization into a GPU code. Here, we solved this model using a dual buffering scheme (Ping-Pong technique) and an optimized use of the different GPU memories [47, 48].

We study how the process of pattern formation varies with the parameter related to the temperature τ , while keeping the rest of the parameters fixed at the following values: $M = 1.0$, $D = 0.1$, $a = 1.5$, $v = 2.3$, $u = 0.38$ and $b = 0.01$. The initial homogeneous (disordered) state is simulated by a random noise distribution of the order parameter.

Figure 3 shows two snapshots of typical pattern configurations obtained through simulations of monolayers, at different conditions of annealing when an initially disordered system is quenched into the spinodal region ($\tau_s < \tau < \tau_{\text{ODT}}$).

To obtain a better comparison with the experimental AFM phase images shown in Fig. 1, rather than considering a contour plot to describe the individual PS spheres, in Fig. 4 we integrate the order parameter describing the density fluctuations along the direction perpendicular to the substrate. In this way, the interfaces are smoothed out, facilitating the comparison with AFM. Note the qualitative agreement between experimental data (Fig. 1) and the numerical results shown in Fig. 4 for systems at different annealing conditions.

ii. Linear Instability Analysis

Due to the strong degree of confinement in the monolayer, in general the formation of ordered structures and patterns can be well approximated as a 2D process. In this section we consider temperatures in the vicinity of the order–disorder transition ($T \lesssim T_{\text{ODT}}$) and study the pattern evolution of a modulated structure in the plane $z = 0$, whose order parameter profile can be described by the following sum of Fourier modes

$$\psi(\mathbf{r}, t) = \sum_{\mathbf{k}} \psi_{\mathbf{k}} \exp(i\mathbf{k} \cdot \mathbf{r} + \lambda t), \quad (9)$$

where $\psi_{\mathbf{k}}$ is the Fourier coefficient at $t = 0$ (we consider that \mathbf{k} is restricted to the thin film's middle plane and neglect the spatial variation of ψ along the direction perpendicular to the thin film surfaces).

The stability of the solution $\psi = 0$ (high temperature phase) for a system quenched into an unstable state can be studied by linearizing Eq. (7) around $\psi = 0$ [49, 50]. Substituting Eq. (9) into the linearized Eq. (7), it can be easily shown that the amplification factor λ satisfies

$$\lambda(k) = -D k^4 + [\tau - a(1 - 2f)^2] k^2 - b, \quad (10)$$

where $k = \|\mathbf{k}\|$. The spinodal/nucleation and growth transition line can be calculated as the lowest value of τ for which an extended mode can grow, i.e., $\lambda > 0$ for some k

$$\tau_s = 2\sqrt{Db} + a(1 - 2f)^2. \quad (11)$$

Thus, for $\tau < \tau_s$, no extended mode can be amplified and the state $\psi = 0$ is a stable or metastable configuration. If $\tau > \tau_s$, some modes grow exponentially with time. These growing modes are constrained according to

$$k_1^2 \leq k^2 \leq k_2^2, \quad (12) \quad \text{with } \Gamma = \tau - a(1 - 2f)^2. \text{ Moreover, the most unstable}$$

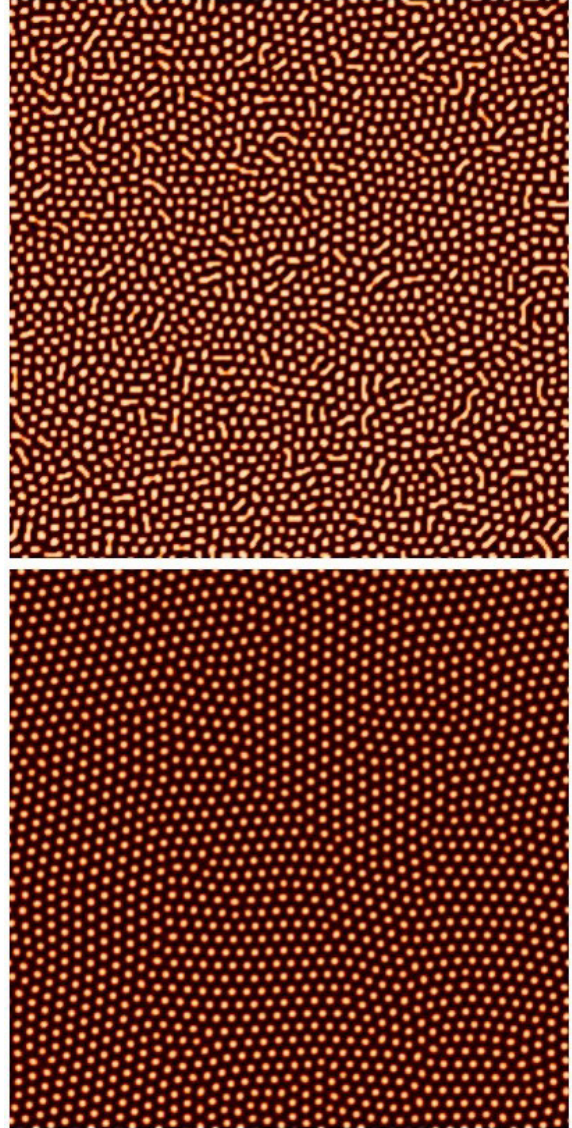


Figure 4: Two-dimensional pattern configurations for the 3D simulation data shown in Fig. 3. Observe the similarities between these patterns and those in the experimental system shown in Fig. 1.

where

$$\begin{aligned} k_1^2 &= \frac{\Gamma - \sqrt{\Gamma^2 - 4Db}}{2D}, \\ k_2^2 &= \frac{\Gamma + \sqrt{\Gamma^2 - 4Db}}{2D}, \end{aligned} \quad (13)$$

mode (where λ is maximal) is

$$k_s = \sqrt{\frac{\Gamma}{2D}}. \quad (14)$$

If $\tau \rightarrow \tau_s$, this has the form $k_s \rightarrow (b/D)^{1/4}$, and is the only mode which is unstable.

Note that, in general, the spinodal temperature does not coincide with the order–disorder transition temperature, T_{ODT} . If a homogeneous system is quenched between these temperatures, it can remain in a metastable state, which can relax only by nucleation and growth. For block copolymers the two temperatures coincide only for symmetric lamellar morphologies, $f = \frac{1}{2}$ [1].

Figure 5 shows the range of unstable modes as given by Eq. (12). Note that the distribution of unstable modes is not symmetrically distributed around k_s , the wave vector at the spinodal. This skewness becomes progressively larger as the depth of quench increases. Consequently, for systems quenched in the neighborhood of the spinodal, one can expect a very strong length scale selectivity and a strong free energy penalty for elastic distortions which shift the system from the optimum k_s . On the other hand, deep quenches stabilize the presence of different elastic distortions and thus, more disordered patterns can be expected. In addition, due to the skewness of the distribution, phase-separated systems generated at deep quenches are characterized by an average wave vector $k > k_s$.

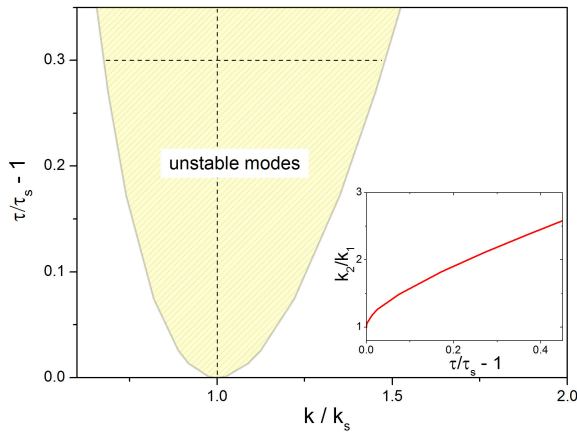


Figure 5: Range of unstable modes as a function of the reduced temperature. Inset: k_2/k_1 as a function of the reduced temperature. Note that the unstable modes are not evenly distributed around k_s .

It is known that the linear instability analysis describes only the initial stage (short times) of the spinodal decomposition mechanism. As time proceeds, the dynamics become highly nonlinear and higher-order wave numbers emerge [51–53]. We will discuss these other stages of spinodal decomposition in the next section.

IV. Results

i. Spinodal Decomposition

Spinodal decomposition is the process of relaxation of thermodynamically unstable states. Early studies on spinodal decomposition date back to the 1960s, with the pioneering works of Cahn and Hilliard [53], Hillert [54], and Lifshitz and Slyozov [55]. Such studies were mainly focused on the mechanism of phase formation and macroscopic phase separation in solid binary alloys and fluid binary mixtures.

At present, it is well known that spinodal decomposition in binary mixtures has three different regimes [56]. Initially, some modulations present in the homogeneous phase grow exponentially with time, following the early linear evolution dynamics. With time, the nonlinear coupling between these growing modes slows their growth. In this second stage, the pattern has well-defined interfaces delimiting domains of the different stable phases. At longer times, the average domain size increases in order to reduce the total interfacial area. The asymptotic long-time state consists of two macroscopic domains, one for each phase.

In block copolymers, most of the studies of pattern formation and ordering investigate the later stage of spinodal decomposition (the coarsening stage), focusing on the kinetic exponents of evolution, and comparison with other related systems, like the self-assembled structures observed in Rayleigh-Benard convection [17, 18, 46, 56–60]. Here, we consider the early stages of spinodal decomposition in sphere-forming block copolymer systems under confinement in monolayers. We have observed two leading factors that control the degree of order during annealing below the spinodal. For $\tau > \tau_s$ the system is nanophase-separated but disordered and the kinetics of ordering are completely inhibited, while for $\tau \gtrsim \tau_s$ the strong length scale selectivity observed in Fig. 5 leads to well-defined hexagonal patterns with a lower density of defects and faster ordering kinetics. The differences in mode selectivity as a function of τ can be visualized in Fig. 3, where it

can be appreciated that deep quenches lead to patterns with poorly defined symmetry.

In order to explore the dynamics and to facilitate comparison with the experimental results, here we have computed the circularly averaged structure factor for both experiments and simulations. The circularly averaged structure factor is defined as

$$S_k = \langle \tilde{\psi}(\mathbf{k}) \tilde{\psi}^*(\mathbf{k}) \rangle, \quad (15)$$

where $\tilde{\psi}(\mathbf{k})$ is the Fourier transform of the order parameter.

For the experimental data, we have calculated S_k through the phase fields obtained by imaging the block copolymer with AFM. Although the density maps obtained by AFM are correlated with the local elasticity of the system, rather than with density fluctuations, they adequately describe the main pattern features: symmetry, defects, and degrees of local and long-range order.

Figure 6 shows S_k for systems quenched and annealed at different conditions, as obtained from the simulations. Here, if the high-temperature phase is deeply quenched into the spinodal region ($\tau_r = \tau/\tau_s - 1 = 0.2$), the length-scale selectivity imposed by the radius of gyration of the molecule leads to a nanophase-separated system with poorly defined symmetry. The insets in Fig. 6 show the 2D scattering function for this system under two different conditions. The broad halo

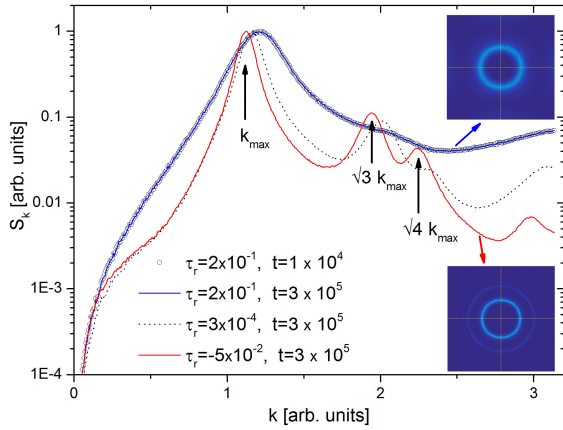


Figure 6: Circularly averaged scattering function S_k from simulations, at different depths of quench and annealing times. The insets show the 2D patterns of S_k . The higher-order peaks, located at $\sqrt{3}k_{\max}$, $\sqrt{4}k_{\max}$ and $\sqrt{7}k_{\max}$, are the signature of hexagonal order.

of intensity is consistent with a poorly defined symmetry and liquid-like order. In this case, there is not only one mode which can grow, but rather a continuous range of modes delimited by an annulus determined by $k_1 \leq k \leq k_2$ (see Fig. 5). As the temperature is low and a wide spectrum of modes is stable, the kinetics of coarsening are frozen. Observe in Fig. 6 that even after 3×10^5 time steps, S_k remains unaffected when $\tau_r = 0.2$. Similar results were found by Yokojima and Shiwa, and by Sagui and Desai, in a related system [61–63]. By including thermal fluctuations it has been shown that the system can move towards equilibrium via defect annihilation and grain growth [17, 64].

When the same system is subjected to a shallow quench, $\tau_r = 3 \times 10^{-4}$, S_k shows the typical features of hexagonal patterns, with a sharper main peak at k_{\max} and well-defined higher-order peaks at $\sqrt{3}k_{\max}$, $\sqrt{4}k_{\max}$ and $\sqrt{7}k_{\max}$. The rings of nearly uniform intensity are also a signature of isotropy. However, in this case the isotropy emerges as a consequence of the polycrystalline structure and not a liquid-like order, as in the case of systems deeply quenched below the spinodal temperature T_S .

The dominant features of the scattering function during spinodal decomposition are in good qualitative agreement with the experimental data shown in Fig. 7. In the experimental system, the early patterns are char-

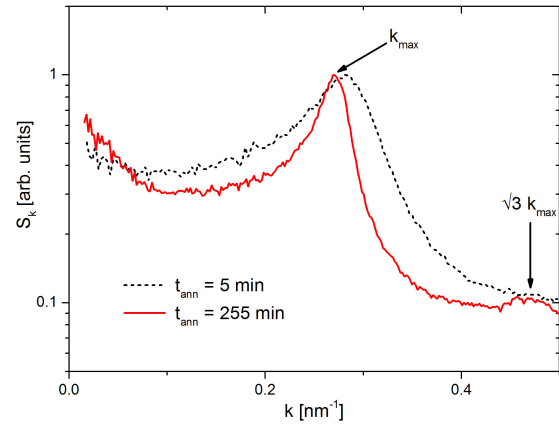


Figure 7: Circularly averaged scattering function S_k for the experimental data at two different annealing times. Annealing temperature: $T=333$ K. Note that as annealing time increases, the main peak sharpens, shifts towards lower values of k , and develops a second-order peak at $\sqrt{3}k_{\max}$, characteristic of a hexagonal pattern.

acterized by a strong length-scale selectivity, but short-range order (see also Fig. 1). As the annealing time increases, there is a shift of the main peak in S_k towards lower values of k . In addition, the main peak sharpens, and a weak higher-order peak located at $\sqrt{3}k_{\max}$ can be clearly identified. These features are in good agreement with the results of Figs. 1 and 2, which show increasing order with annealing time.

Although there is qualitative agreement between experiments and simulations, it must be emphasized that the model employed here cannot capture the detailed dynamics of the system as a function of temperature. In block copolymers, the chain mobility depends on an effective monomeric friction coefficient that is strongly dependent on temperature, the glass transition and/or crystallization temperatures of the individual blocks, the degree of segregation between blocks, the symmetry of the self-assembled structure, and the degree of entanglement. Although some of these properties can be qualitatively captured through an effective mobility coefficient [M in Eq. (1)], at present it is not quantitatively clear how these factors affect the dynamics.

ii. Nucleation and growth

When the high-temperature phase is quenched to temperatures slightly above the spinodal (quenches with $\tau \lesssim \tau_s$), all the modes decrease exponentially in time and the order parameter goes to zero across the whole system. That is, the initially randomly distributed order parameter $\psi(\mathbf{r})$, characterized by $\langle \psi(\mathbf{r}) \rangle = 0$ and $\langle \psi(\mathbf{r})\psi(\mathbf{r}') \rangle \neq 0$, dies off. However, in the same range of temperatures, an initial crystalline hexagonal pattern is completely stable, indicating a region of metastability $\tau_s > \tau > \tau_{\text{ODT}}$, where τ_{ODT} denotes the limit of metastability.

In addition, within this metastable region, a polycrystalline structure can improve its degree of order via the annihilation of defects, with a similar mechanism to the one observed for quenches only slightly below the spinodal. Figure 6 also shows S_k for a system quenched into this metastable region ($\tau_s > \tau > \tau_{\text{ODT}}$, $\tau_r = -5 \times 10^{-2} < 0$). Note that at the same time of annealing (3×10^5 timesteps), as compared with the system quenched below the spinodal ($\tau_r = 3 \times 10^{-4} > 0$), this system shows an improved order, as the main peak sharpens and higher-order peaks become better defined.

The most distinctive feature of the metastable region is that only the nuclei or grains above a critical size can grow to develop the equilibrium phase, while smaller

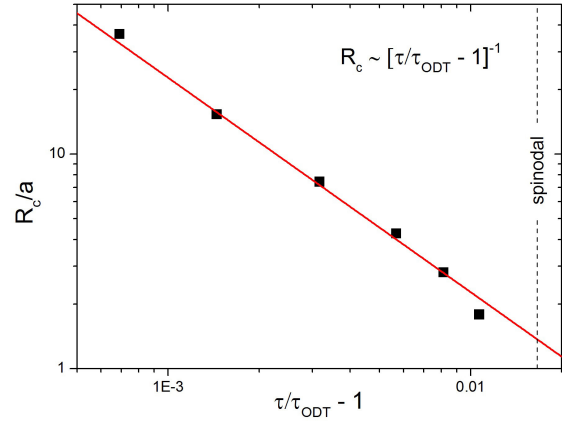


Figure 8: Critical nucleus size R_c vs. the reduced temperature $\tau/\tau_{\text{ODT}} - 1$. Here a is the lattice constant. Note that $R_c \sim a$ for $\tau \sim \tau_s$.

nuclei collapse due to the surface free energy. According to the classical picture of nucleation and growth in 2D, the variation in the free energy ΔF due to the formation of a nucleus of radius R can be expressed as [21, 22]

$$\Delta F = 2\sigma\pi R - \pi|\Delta F_0|R^2, \quad (16)$$

where σ represents the line tension and $\Delta F_0 \propto (\tau_{\text{ODT}} - \tau)$ is the difference in the local free energies of the high-temperature (disordered) and the low-temperature (ordered) phases, which drives the transition. Due to the competition between these surface and volume contributions, only those nuclei whose size exceeds a critical value R_c can propagate to form the equilibrium phase.

In order to obtain the dependence of the critical size for nucleation R_c on the depth of quench, we explore the stability of crystalline nuclei of different sizes.

To study the stability of a crystal seed, we change τ back and forth around the critical value to obtain a defect-free crystal patch. The partial melting and recrystallization involved in this process removes defects and long-wavelength elastic distortions and yields a crystal seed that is then used as an initial condition in the numerical solution of Eq. (1). Figure 8 shows the critical size for nucleation R_c as a function of τ . Around the order–disorder temperature τ_{ODT} we found that the critical size for grain growth R_c diverges as $R_c \sim 1/(\tau/\tau_{\text{ODT}} - 1)$, in agreement with classical the-

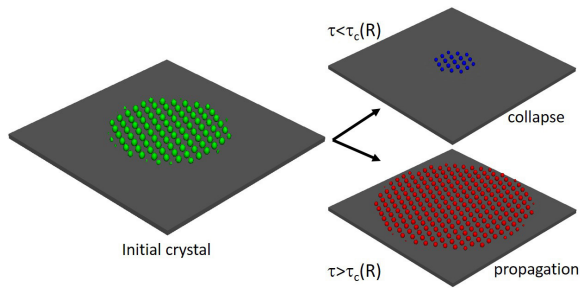


Figure 9: Time evolution of a crystalline domain as a function of temperature for a system quenched to $\tau_{\text{ODT}} < \tau < \tau_s$. Here the left panel corresponds to a hexagonal grain of initial size $R_0/a = 4.6$, where a is the lattice constant. The right panels correspond to a grain that collapses [top, $\tau < \tau_c(R)$] or propagates [bottom, $\tau > \tau_c(R)$].

ories of nucleation and growth [22]. Note also that as the spinodal temperature is approached, the critical size for nucleation becomes on the order of the lattice constant a . This result indicates that the process of spinodal decomposition could be inhibited, as the nucleation and growth process precedes spinodal decomposition [22].

Figure 9 shows typical snapshots of the evolution of nuclei as a function of temperature for quenches within the metastable region ($\tau_{\text{ODT}} < \tau < \tau_s$). For an initial crystalline nucleus of a given size R , and with $R_c \propto (\tau_{\text{ODT}} - \tau)^{-1}$, if the temperature is lowered to a value where R is larger than R_c , grain growth occurs. Otherwise, the crystal collapses since line tension overcomes the bulk contribution.

iii. Melting

A perfect crystalline structure may get trapped in a superheated state, such that the system may remain ordered when annealing above τ_{ODT} . However, we observed that for polycrystalline structures, topological defects trigger the phase transition, inhibiting superheating and disordering the system when $\tau \gtrsim \tau_{\text{ODT}}$. Figure 10 shows a polycrystalline structure obtained during annealing at $\tau_r = 1.64 \times 10^{-2}$. This figure shows the local orientation of the different hexagonal grains and also the defect structure. In 2D crystals with hexagonal symmetry, the elementary defects, named disclinations, are the domains which have a number of neighbors different from six (a five-coordinated domain is a positive disclination and a seven-coordinated domain is a negative disclination). In general, these de-

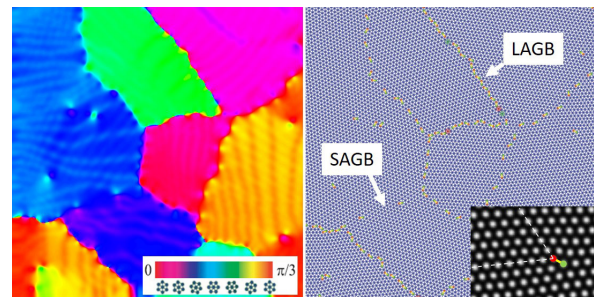


Figure 10: Orientational map $\theta(\mathbf{r})$ (left panel) and defect structure (right panel) of the hexagonal lattice determined by a Delaunay triangulation. Spheres with seven neighbors are indicated with a green dot, those with five neighbors in red. Dislocations are formed by a pair of 5-7 disclinations separated by one lattice constant, and are indicated by a connecting yellow line segment (see also the inset with a dislocation). A comparison between the defect structure and local orientation indicates that grain boundaries are decorated with linear arrays of dislocations. The bottom of the figure for $\theta(\mathbf{r})$ shows the color scale used to indicate the local orientation. Here the patterns correspond to $\tau_r = 1.64 \times 10^{-2}$ and 9×10^4 time steps.

fects are too energetic to be found in isolation: they couple in pairs to form dipoles, also known as dislocations (see Fig. 10). Note in Fig. 10 that dislocations are piled up in linear arrangements, decorating the grain boundaries. Figure 11 shows two snapshots of the system during annealing at temperatures above T_{ODT} . Note in this figure the strong correlation between the liquid-like phase ($\psi = 0$) and the position of the initial grain boundaries. In addition, it can also be observed that melting does not start uniformly at all grain boundaries, but depends on the orientational mismatch between neighboring crystals.

The average distance between the dislocations located along a grain boundary depends on the orientation mismatch between neighboring grains, $\Delta\theta$, as $d_{ds} \propto a/\Delta\theta^{-1}$, where a is the lattice constant. Note that the largest possible mismatch in orientation between crystals in a hexagonal pattern is 30 Degrees. Compared with small-angle grain boundaries (SAGB), large-angle grain boundaries (LAGB, those for which the orientational mismatch is in the range 10–30 Degrees), are more energetic and contain a larger number of dislocations per unit length. Consequently, the phase transition is initially triggered at LAGB, where the crystal is more disordered. We also observe that the

kinetics of disordering are affected by the initial defect structure. Note in Fig. 12 that a polycrystal with small crystal size, and thus a higher content of dislocations, leads to a larger fraction of the liquid phase at the same annealing time.

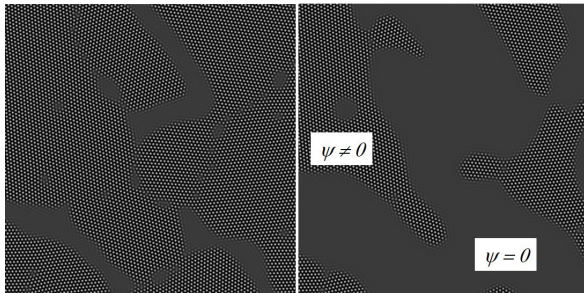


Figure 11: Upon increasing the temperature above T_{ODT} , the crystals of Fig. 10 melt first at LAGB (left panel). As time proceeds, the liquid phase ($\psi = 0$) propagates through the system. $\tau = 0.938\tau_s$. Left panel: $t = 1.5 \times 10^3$ time steps. Right panel: $t = 5 \times 10^4$ time steps.

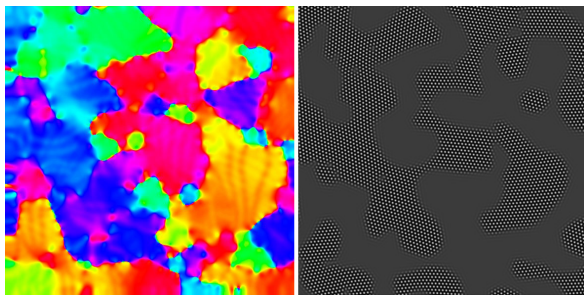


Figure 12: Melting of the crystal phase for a system containing a relatively large initial content of topological defects (left panel). Although the temperature and annealing time are the same as in the left panel of Fig. 11, due to the larger initial content of defects, there is a larger fraction of liquid phase here. $\tau = 0.938\tau_s$, $t = 1.5 \times 10^3$ time steps.

V. Conclusion

In this work, we studied the different mechanisms leading to the self-assembly of sphere-forming block copolymer thin films. Using a Cahn–Hilliard free energy model valid for diblock copolymers, we followed the evolution of the system with numerical simulations for different temperatures, and presented a unified view of the phase transition process. The results are consistent with a first-order transition. Below a spinodal

temperature T_S , the initially homogeneous disordered state relaxes towards equilibrium by spinodal decomposition, by the spontaneous growth of characteristic modes. Above this temperature, the system can only self-assemble into an ordered phase by nucleation and growth ($T_S < T < T_{ODT}$). Above the order–disorder temperature T_{ODT} a well-ordered system can in principle remain superheated without disordering. However, dislocations and grain boundaries trigger the melting of the structure, such that defective states cannot be superheated above T_{ODT} .

For systems quenched into the metastable region, we found that the critical size for nucleation and growth diverges as the disorder–order temperature is approached, following the law: $R_c \sim 1/(\tau/\tau_{ODT} - 1)$, in agreement with classical theories of nucleation and growth.

Acknowledgments

We gratefully acknowledge financial support from the National Science Foundation MRSEC Program through the Princeton Center for Complex Materials (DMR-1420541), Universidad Nacional del Sur and the National Research Council of Argentina (CONICET). The PS-PEP block copolymer was hydrogenated by John Sebastian.

- [1] I W Hamley, *The physics of block copolymers*, Oxford University Press (1998).
- [2] F S Bates, G H Fredrickson, *Block copolymers—designer soft materials*, *Phys. Today* **52**, 32 (1999).
- [3] I W Hamley, *Nanostructure fabrication using block copolymers*, *Nanotechnology* **14**, R39 (2003).
- [4] T P Lodge, *Block copolymers: past successes and future challenges*, *Macromol. Chem. Phys.* **204**, 265 (2003).
- [5] A V Ruzette, L Leibler, *Block copolymers in tomorrow's plastics*, *Nat. Mater.* **4**, 19 (2005).
- [6] R A Segalman, *Patterning with block copolymer thin films*, *Mat. Sci. Eng. R*, **48**, 191 (2005).
- [7] S B Darling, *Directing the self-assembly of block copolymers*, *Prog. Polym. Sci.* **32**, 1152 (2007).

- [8] H C Kim, S M Park, W D Hinsberg, *Block copolymer based nanostructures: Materials, processes, and applications to electronics*, Chem. Rev. **110**, 146 (2010).
- [9] C M Bates, M J Maher, D W Janes, C J Ellison, C G Willson, *Block copolymer lithography*, Macromolecules **47**, 2 (2014).
- [10] M J Fasolka, A M Mayes, *Block copolymer thin films: Physics and applications*, Annu. Rev. Mater. Res. **31**, 323 (2001).
- [11] C Harrison, D H Adamson, Z D Cheng, J M Sebastian, S Sethuraman, D A Huse, R A Register, P M Chaikin, *Mechanisms of ordering in striped patterns*, Science **290**, 1558 (2000).
- [12] C Harrison, Z D Cheng, S Sethuraman, D A Huse, P M Chaikin, D A Vega, J M Sebastian, R A Register, D H Adamson, *Dynamics of pattern coarsening in a two-dimensional smectic system*, Phys. Rev. E **66**, 011706 (2002).
- [13] M L Trawick, M Megens, C Harrison, D E Angelescu, D A Vega, P M Chaikin, R A Register, D H Adamson, *Correction for piezoelectric creep in scanning probe microscopy images using polynomial mapping*, Scanning **25**, 1 (2003).
- [14] A P Marencic, M W Wu, R A Register, P M Chaikin, *Orientalional order in sphere-forming block copolymer thin films aligned under shear*, Macromolecules **40**, 7299 (2007).
- [15] A P Marencic, D H Adamson, P M Chaikin, R A Register, *Shear alignment and realignment of sphere-forming and cylinder-forming block-copolymer thin films*, Phys. Rev. E **81**, 011503 (2010).
- [16] C Harrison, D E Angelescu, M Trawick, Z D Cheng, D A Huse, P M Chaikin, D A Vega, J M Sebastian, R A Register, D H Adamson, *Pattern coarsening in a 2D hexagonal system*, Europhys. Lett. **67**, 800 (2004).
- [17] D A Vega, C K Harrison, D E Angelescu, M L Trawick, D A Huse, P M Chaikin, R A Register, *Ordering mechanisms in two-dimensional sphere-forming block copolymers*, Phys. Rev. E **71**, 061803 (2005).
- [18] L R Gómez, E M Vallés, D A Vega, *Lifshitz-Safran coarsening dynamics in a 2D hexagonal system*, Phys. Rev. Lett. **97**, 188302 (2006).
- [19] N A García, R A Register, D A Vega, L R Gómez, *Crystallization dynamics on curved surfaces*, Phys. Rev. E **88**, 012306 (2013).
- [20] W Li, F Qiu, Y Yang, A C Shi, *Ordering dynamics of directed self-assembly of block copolymers in periodic two-dimensional fields*, Macromolecules **43**, 1644 (2010).
- [21] P M Chaikin, T C Lubensky, *Principles of condensed matter physics*, Cambridge University Press (1995).
- [22] P G Debenedetti, *Metastable liquids*, Princeton University Press (1996).
- [23] J M Sebastian, C Lai, W W Graessley, R A Register, *Steady-shear rheology of block copolymer melts and concentrated solutions: Disorder-stress in body-centered-cubic systems*, Macromolecules **35**, 2707 (2002).
- [24] D E Angelescu, C K Harrison, M L Trawick, R A Register, P M Chaikin, *Two-dimensional melting transition observed in a block copolymer*, Phys. Rev. Lett. **95**, 025702 (2005).
- [25] D E Angelescu, J H Waller, D H Adamson, P Deshpande, S Y Chou, R A Register, P M Chaikin, *Macroscopic orientation of block copolymer cylinders in single-layer films by shearing*, Adv. Mater. **16**, 1736 (2004).
- [26] D E Angelescu, J H Waller, R A Register, P M Chaikin, *Shear-induced alignment in thin films of spherical nanodomains*, Adv. Mater. **17**, 1878 (2005).
- [27] A Adland, Y Xu, A Karma, *Unified theoretical framework for polycrystalline pattern evolution*, Phys. Rev. Lett. **110**, 265504 (2013).
- [28] G H Fredrickson, F S Bates, *Dynamics of block copolymers: Theory and experiment* Annu. Rev. Mater. Sci. **26**, 501 (1996).
- [29] M Doi, S F Edwards, *The theory of polymer dynamics*, Clarendon Press (1986).

- [30] D A Vega, J M Sebastian, Y L Loo, R A Register, *Phase behavior and viscoelastic properties of entangled block copolymer gels*, J. Polym. Sci. Part B: Polym. Phys. **39**, 2183 (2001).
- [31] L Leibler, *Theory of microphase separation in block copolymers*, Macromolecules **13**, 1602 (1980).
- [32] T Ohta, K Kawasaki, *Equilibrium morphology of block copolymer melts*, Macromolecules **19**, 2621 (1986).
- [33] M Serral, M Pinna, A V Zvelindovsky, J B Avalos, *Cell dynamics simulations of sphere-forming diblock copolymers in thin films on chemically patterned substrates*, Macromolecules **49**, 1079 (2016).
- [34] I W Hamley, *Cell dynamics simulations of block copolymers*, Macromol. Theory Simul. **9**, 363 (2000).
- [35] S R Ren, I W Hamley, *Cell dynamics simulations of microphase separation in block copolymers*, Macromolecules **34**, 116 (2001).
- [36] N Provatas, K Elder, *Phase-field methods in material science and engineering*, Wiley (2010).
- [37] L R Gómez, D A Vega, *Amorphous precursors of crystallization during spinodal decomposition*, Phys. Rev. E **83**, 021501 (2011).
- [38] Y Guo, J Zhang, B Wang, H Wu, M Sun, J Pan, *Microphase transitions of block copolymer/homopolymer under shear flow*, Condens. Matter Phys. **18**, 23801 (2015).
- [39] A D Pezzutti, L R Gómez, D A Vega, *Smectic block copolymer thin films on corrugated substrates*, Soft Matter **11**, 2866 (2015).
- [40] S K Mkhonta, K R Elder, Z F Huang, *Emergence of chirality from isotropic interactions of three length scales*, Phys. Rev. Lett. **116**, 205502 (2016).
- [41] T Ohta, Y Enomoto, J L Harden, M Doi, *Anomalous rheological behavior of ordered phases of block copolymers. I*, Macromolecules **26**, 4928 (1993).
- [42] M Nonomura, *Stability of the fcc structure in block copolymer systems*, J. Phys.: Condens. Matter **20**, 465104 (2008).
- [43] K Yamada, S Komura, *The dynamics of order-order phase separation*, J. Phys.: Condens. Matter **20**, 155107 (2008).
- [44] R Choksi, X Ren, *On the derivation of a density functional theory for microphase separation of diblock copolymers*, J. Stat. Phys. **113**, 151 (2003).
- [45] A A Abate, G T Vu, A D Pezzutti, N A García, R L Davis, F Schmid, R A Register, D A Vega, *Shear-aligned block copolymer monolayers as seeds to control the orientational order in cylinder-forming block copolymer thin films*, Macromolecules **49**, 7588 (2016).
- [46] G J A Sevink, *Rigorous embedding of cell dynamics simulations in the Cahn–Hilliard–Cook framework: Imposing stability and isotropy*, Phys. Rev. E **91**, 053309 (2015).
- [47] J Nickolls, I Buck, M Garland, K Skadron, *Scalable parallel programming with CUDA*, ACM Queue **6**, 40 (2008).
- [48] NVIDIA, *CUDA Programming Guide 8.0*, <http://docs.nvidia.com/cuda/> (2017).
- [49] D A Vega, L R Gómez, *Spinodal-assisted nucleation during symmetry-breaking phase transitions*, Phys. Rev. E **79**, 051607 (2009).
- [50] A D Pezzutti, L R Gómez, M A Villar, D A Vega, *Defect formation during a continuous phase transition*, Europhys. Lett. **87**, 66003 (2009).
- [51] J W Cahn, *The later stages of spinodal decomposition and the beginnings of particle coarsening*, Acta Met. **14**, 1685 (1966).
- [52] J S Langer, M Bar-on, H D Miller, *New computational method in the theory of spinodal decomposition*, Phys. Rev. A **11**, 1417 (1975).
- [53] J W Cahn, J E Hilliard, *Free energy of a nonuniform system. I Interfacial free energy*, J. Chem. Phys. **28**, 258 (1958).
- [54] M Hillert, *A solid-solution model for inhomogeneous systems*, Acta Met. **9**, 525 (1961).

- [55] I M Lifshitz, V V Slyozov, *The kinetics of precipitation from supersaturated solid solutions*, J. Phys. Chem. Solids **19**, 35 (1961).
- [56] A J Bray, *Theory of phase-ordering kinetics*, Adv. Phys. **43**, 357 (1994).
- [57] Y Oono, S Puri, *Computationally efficient modeling of ordering of quenched phases*, Phys. Rev. Lett. **58**, 836 (1987).
- [58] Y Oono, M Bahiana, *2/3-Power law for copolymer lamellar thickness implies a 1/3-power law for spinodal decomposition*, Phys. Rev. Lett. **61**, 1109 (1988).
- [59] F Liu, N Goldenfeld, *Dynamics of phase separation in block copolymer melts*, Phys. Rev. A **39**, 4805 (1989).
- [60] M Bahiana, Y Oono, *Cell dynamical system approach to block copolymers*, Phys. Rev. A **41**, 6763 (1990).
- [61] Y Yokojima, Y Shiwa, *Hydrodynamic interactions in ordering process of two-dimensional quenched block copolymers*, Phys. Rev. E **65**, 056308 (2002).
- [62] C Sagui, R C Desai, *Kinetics of topological defects in systems with competing interactions*, Phys. Rev. Lett. **71**, 3995 (1993).
- [63] C Sagui, R C Desai, *Late-stage kinetics of systems with competing interactions quenched into the hexagonal phase*, Phys. Rev. E **52**, 2807 (1995).
- [64] L R Gómez, E M Vallés, D A Vega, *Effect of thermal fluctuations on the coarsening dynamics of 2D hexagonal system*, Physica A **386**, 648 (2007).